Journal of Oceanography (2023) 79:445–460
https://doi.org/10.1007/s10872-023-00687-4

ORIGINAL ARTICLE

Near-surface dynamic structure in the northern South China Sea and Northwest Pacific revealed using Lagrangian data

Pengchao Niu[1] · **Guanghong Liao**[1,2]

Received: 28 June 2022 / Revised: 15 March 2023 / Accepted: 18 March 2023 / Published online: 1 April 2023

Abstract

The Northwest Pacific region is one of the most energetic in the near-inertial frequency band. Owing to the impacts of significant monsoon and the Kuroshio, the local dynamic environment of the northern South China Sea (SCS) and Northwest Pacific is complicated, and the inertial motions exhibit temporal and spatial variabilities. By fitting the complex velocity spectrum of the Lagrangian time series derived from the Global Drifter Program data using a Lagrangian stochastic model, which combines the complex-valued Ornstein–Uhlenbeck and Matérn processes, the main characteristics of near-inertial oscillations (NIOs) and mesoscale turbulence were extracted and analyzed. The integral near-inertial variance (NIV) is related to the amplitude and damping parameters. Fitted high energy spectrum is determined by small amplitude and large damping parameter or large amplitude and small damping parameter. It was found that the pattern of NIV of NIOs is consistent with the strength of wind fluctuation, and the strongest NIV present in the Luzon strait and northern SCS. The frequency shift in NIOs is related to background vorticity and damping timescale. The large geostrophic turbulent amplitude presents along with the Kuroshio path. The decorrelation timescale in the northern SCS is lower than that in the Philippine Sea, and the motions in northern SCS are more approaching to white noise. The isotropic diffusivity is higher along the Kuroshio path, accompanied with the energetic geostrophic turbulent.

Keywords Lagrangian stochastic model · Inertial oscillation · Geographic turbulence · Dynamic structure; surface drifters

1 Introduction

Oscillations occurring near local inertial frequency, known as near-inertial oscillations (NIOs) and mainly driven by strong surface wind, tropical cyclones (Pollard and Millard 1970), are common in the upper ocean (Alford et al. 2016; Ferrari and Wunsch 2009). Rapid changes in wind stress induce a near-inertial motion, which can easily resonate with the NIOs of the mixed layer when the frequency of wind is close to that of the local inertia (D'asaro 1989). NIOs propagation is influenced by oceanic mesoscale background processes, such as eddies and loop currents (Mooers 1973; Shay et al. 1998). The blue and red shifts in the inertial frequency are related to background vorticity (Sun et al. 2011b). Downward-propagating inertial oscillation ultimately dissipates into microscale turbulent mixing because of nonlinear wave–wave interaction (Alford et al. 2016). Therefore, NIOs are indispensable for multi-scale dynamic processes and energy budget in ocean. According to Munk and Wunsch (1998), 2.1 TW of maintaining the oceanic mixed energy, 0.9 TW from internal tide, 1.2 TW input from the wind field. Near-inertial oscillations caused by the rapid change of wind stress and their induced mixing play an important role in maintaining the global thermohaline circulation.

Park et al. (2005) presented a global map of inertial amplitude in which they suggested that the amplitude in summer is great than that in winter by15%–25%. Elipot et al. (2010) argued that the largest values of near-inertial variance (NIV) are found at midlatitudes in all basins, under the atmospheric storm tracks. These regions include the midlatitudes of the North Pacific and Kuroshio extension region. Chaigneau et al. (2008) indicated that wind-driven NIOs are occur at greater frequency during fall and winter,

✉ Guanghong Liao
liaogh@hhu.edu.cn

[1] Key Laboratory of Marine Hazards Forecasting, Ministry of Natural Resources, Hohai University, Nanjing China, Nanjing 210098, China

[2] Laboratory for Regional Oceanography and Numerical Modeling, Pilot National Laboratory for Marine Science and Technology, Qingdao 266000, China

associated with maximum storm activity and deeper mix layers. In addition, Sun et al. (2019) studied near-inertial oscillations in the South China Sea (SCS) and found that different data methods can impact the results; thus, analyzing the sensitivity of the NIOs to methods is vital.

Single-point Euler devices cannot accurately reflect the large-scale spatial characteristics of NIV owing to the limitations of the number of devices deployed and fixed location (Qian et al. 2013). Therefore, Lagrangian devices with a greater range of spatial coverage and higher distribution cost-effectiveness are being increasingly used to study NIOs (Lacasce 2008; Park et al. 2004). Over previous decades, increased availability of Lagrangian observations using subsurface floats and surface drifters has facilitated research on Lagrangian statistics over oceans Park et al. (2009) estimated the global distribution of mixed layer inertial amplitude used satellite-tracked drifters. Eulerian and Lagrangian statistics of surface flows over the SCS basin based on observations from satellite-tracked drifters is investigated by Qian et al. (2013). The results revealed that the NIV peaks are in the southern Indian Ocean, the Southern Ocean, and the Luzon Strait. Capturing spatial and temporal structures in high-dimensional datasets is an essential theme in modern statistics (Davis et al. 2013; Guinness and Stein 2013).

The Northwest Pacific is one of the most energetic regions in the near-inertial frequency band (Chaigneau et al. 2008), with a high incidence of typhoons globally, solid response to tropical cyclones, and a complex ocean current system. The SCS, connected to the Northwest Pacific via the Luzon Strait, is one of the largest marginal seas in the Northwest Pacific (Sun et al. 2011a). A complex coastline and numerous island bays cause extreme complications in the multi-scale dynamic processes of the SCS (Wang et al. 2010; Zheng et al. 2008). Previous studies on NIOs features and seasonal variations in the upper ocean of the region relied mostly on moored records, satellite data, and numerical models (Chen et al. 2013; Li et al. 2015; Sun et al. 2019).

Beside inertial peak feature, another major component commonly observed in oceanic data is a red background process, reflecting the mesoscale turbulent flow. Mesoscale fluctuations are almost always and anywhere presented in the ocean, and they are ubiquitous and important for many aspects of the large-scale ocean circulation and often are referred to as oceanic mesoscale eddies or geostrophic turbulence. And the mesoscale fluctuations have spatial scales around the first baroclinic Rossby radius and time scales ranging from the inertial period to several weeks or at most months and are dynamically well described by the quasi-geostrophic approximation. Mesoscale turbulence parameterizations are crucial for climate applications of ocean general circulation models (OGCMs). Lagrangian instruments are particularly suitable for transport and mixing studies because they move approximately with the ocean currents on (sub) mesoscale time scales. This is the idea behind stochastic models. Veneziani et al. (2004) analyzed 700-m acoustically tracked floats in northwestern Atlantic Ocean, and found that the properties of Lagrangian data can be considered as a superposition of two different regimes associated with looping and non-looping trajectories and that both regimes can be parameterized using a simple first-order Lagrangian stochastic model. Another several stochastic models have also been proposed to simulate low-frequency turbulent flow, see LaCasce (2008) for a review. The proposed models are all integer order, and assumed that the velocity or the acceleration is a Markovian process, which is not correspond to field observation (Rupolo et al. 1996). Recently, Sykulski et al. (2016) proposed a Lagrangian time series model, which is consists of complex-valued Ornstein–Uhlenbeck (OU) process and Matérn process, and the former is used to infer important physical parameters of inertial oscillations, and the letter explores turbulent dispersion of geostrophic turbulence. The Matérn process is found to provide an excellent match to modeling velocities from particle trajectories in an application to two-dimensional fluid turbulence (Lilly et al. 2017).

The goal of this work is to characterize the main properties of the NIOs and mesoscale turbulence by Lagrangian stochastic model capable of describing them. This paper is organized as follows. Section 2 first introduces the Global Drifter Program (GDP) datasets. An improved Lagrangian stochastic model proposed recently by Sykulski et al. (2016) is reviewed, and especially focus on physical meaning of model parameter. In Sect. 3, mean current and inferred from Lagrangian data and Kuroshio intrusion features is firstly analyzed. The extracting of dynamical parameters for NIOs and geostrophic turbulence process from a drifter using LSM is given in detail, and then their spatial distribution and seasonal variation are investigated. Section 4 concludes the paper.

2 Data and method

2.1 Drifter dataset

The Global Drifter Program (GDP) is the principal component of the Global Surface Drifting Buoy Array, a branch of the Global Ocean Observing System deployed by the National Oceanic and Atmospheric Administration (NOAA), and a scientific project of the Data Buoy Cooperation Panel. In total, greater than 13,000 near-surface satellite-tracked drifter trajectories have been deployed since 1979. NOAA's Atlantic Oceanographic and Meteorological Laboratory coordinates the deployments, processes and archives the data, maintains metadata files describing each drifter deployed, and develops and distributes data-based products.

Drifters are fixed 15 m underwater with a holey-sock drogue to reduce their drifting from position because of wind and waves (Lumpkin et al. 2017). The drifters move with the mixed layer sea current, and the position information of their floats located on the sea surface is transmitted to the satellite (Lumpkin et al. 2007). The trajectories are interpolated at 1 h intervals, and velocity components are computed using the Lumpkin method. In this study, we extracted a subset of drifters covering the northern SCS and the Northwest Pacific (15–35°N, 110–140°E).

Figure 1a displays the array of surface trajectories of drifters in the northern SCS and Northwest Pacific Ocean. Most of the drifters entered the SCS via the Luzon Strait, which is a high-density drifter area related to the Kuroshio intrusion. These drifters followed the northern SCS currents that moved westward to the east of Vietnam. Other drifters in the Luzon Strait reached Japan from the Philippines along the Kuroshio path. The number of drifter observations are presented in Fig. 1b. Only drifters containing greater than 100 observations were considered statistically valid for representativeness. From Fig. 1b, we can observe that the Luzon Strait region exhibits heavy drifter sampling. The drifters selected for this study cover a large time range, and the distribution and number of drifters satisfied our requirements.

The earliest drifter of GDP was deployed in 1979. However, no compelling drifter observations were recorded in the region until 2003, after which the data started increasing significantly, and the maximum observation data values in 2011 exceeded 110 000 (Fig. 2a). There are seasonal variations in data distribution, with the maximum observations in winter (Fig. 2b).

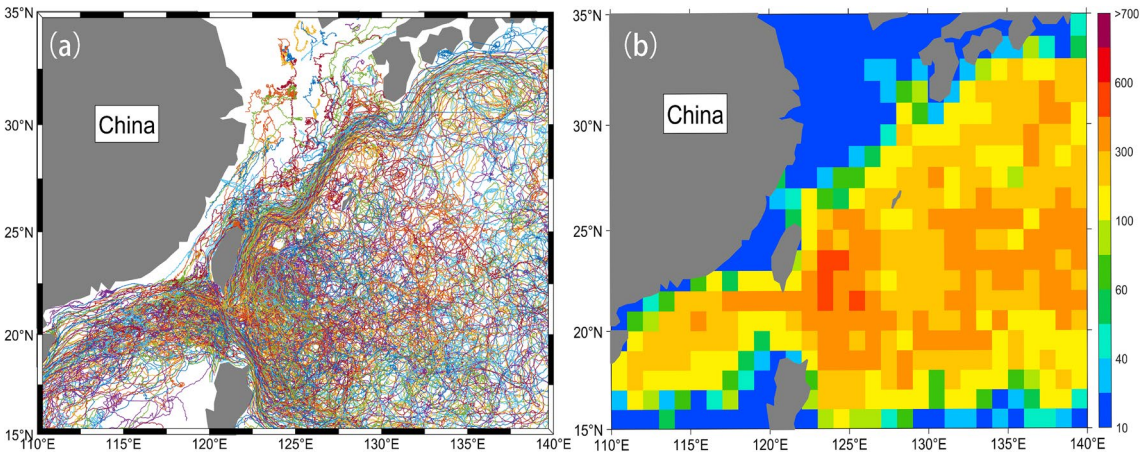

Fig. 1 **a** Drifter trajectories of 1 h drifters in the region (15–35°N, 110–140°E); **b** numbers of drifter samples in 1° × 1° bins

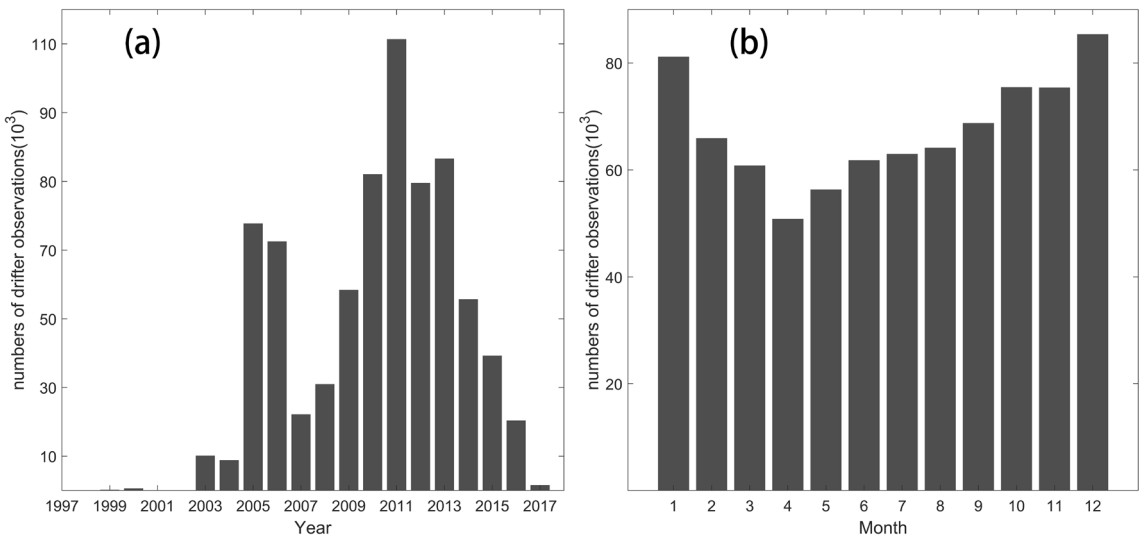

Fig. 2 Temporal distribution of the number of drifter observations as a function of **a** year and **b** calendar month within the region in Fig. 1

2.2 Lagrangian stochastic model

The use of stochastic processes to study Lagrangian times series is common in oceanography (Griffa et al. 2008; LaCasce 2008; Veneziani et al. 2004). In the early oceanographic studies, the analysis of Lagrangian data is primarily restricted to nonparametric estimates of the first-order and second-order moments of the velocity time series (LaCasce 2008). Recently, an alternative physically motivated stochastic Lagrangian stochastic model (LSM) is proposed by Sykulski et al. (2016), which seek to build statistical models using knowledge of the anticipated physical structure in the data.

The LSM involves two key physical ocean processes: the inertial oscillation and the turbulent background. The most of the properties of inertial oscillations observed near the ocean surface is governed by a set of coupled ordinary differential equations (Pollard and Millard 1970).

$$\frac{\partial u}{\partial t} - fv = F - cu$$

$$\frac{\partial v}{\partial t} + fu = G - cv, \tag{1}$$

where u and v, respectively, correspond to the eastward and northward velocities. F and G are time-varying forcing functions associated with surface winds, linear damping term $-cu$ models the dispersion effect by introducing a decay factor of the form exp $(-c(t))$. c^{-1} is referred to as the e-folding time. The parameter f is the Coriolis frequency. The complex-valued velocity $z(t) = u(t) + iv(t)$ is governed by the stochastic different equation

$$dz(t) = \big(i\omega_f(t) - c(t)\big)z(t)dt + AdQ(t)\,, \tag{2}$$

where $dQ(t)$ represent an idealized stochastic model for the wind forcing, combining the effects of F and G from the above inertial oscillation equation. The parameter $\omega_f(t)$ dictates the frequency of the inertial oscillation, which varies with the changing drifter location. The damping parameter $c > 0$ ensures the process is guaranteed to eventually return to its expected value from any initial condition. Finally, $A > 0$ sets the magnitude of the variability, and reflects the strength of the surface wind stress forcing. Equation (2) is recognized as the complex Ornstein–Uhlenbeck (OU) process. The autocovariance function and power spectral density of the continuous-time complex OU process with stationary initial conditions are found to be Sykulski et al (2016)

$$s^{(\mathrm{ou})}(\tau) = E\{z(t)z^*(t+\tau)\} = \frac{A^2}{2c}e^{i\omega_f\tau}e^{-c|\tau|} \tag{3}$$

$$S^{(\mathrm{ou})}(\omega, t) = \frac{A(t)^2}{\big(\omega-\omega_f(t)\big)^2+c(t)^2}\,, \tag{4}$$

where E is the expectation operator, and $z^*(t)$ is the complex conjugate of $z(t)$. The autocovariance $s^{(\mathrm{ou})}(\tau)$ decays exponentially. The power spectral density $S^{(\mathrm{ou})}(\omega, t)$ forms a Fourier pair with the autocovariance and decay in frequency proportionally to $\left|\omega - \omega_f\right|^2$ for $\left|\omega - \omega_f\right| \gg c$. The inertial oscillation model will only be used to capture spectral energy that is localized around the inertial peak; the rest of the spectrum will be captured by a model for the turbulent background.

A second major component commonly observed in Lagrangian data is a red background process, reflecting the large-scale turbulent flow of the ocean currents. Several stochastic models have already been proposed to simulate dispersion, calculate Lagrangian frequency spectra and examine the relation between Lagrangian and Eulerian integral scales (Berloff and Mcwilliams 2002; LaCasce 2008). The previous proposed models are all integer order, and is assumed as a Markovian process, such as Brownian motion or the OU process. However, the spectral slopes of Lagrangian velocities do not correspond to the power of an even integer (Rupolo et al. 1996). This suggests the use of fractional, instead of Markovian, processes to model the background, is more reasonable. The complex-valued Matérn process is used to model background velocities in the LSM proposed by Sykulski et al. (2016). The autocovariance function and power spectral density for complex-valued Matérn process is defined (Sykulski et al. 2016)

$$s^{(\mathrm{m})}(\tau) = \frac{B^2\pi^{0.5}}{2^{\alpha-1.5}\Gamma(\alpha)h^{2\alpha-1}}(h|\tau|)^{\alpha-0.5}\kappa_{\alpha-0.5}(h|\tau|) \tag{5}$$

$$S^{(\mathrm{ma})}(\omega, t) = \frac{B^2(t)}{\big(\omega^2+h^2(t)\big)^{\alpha(t)}}\,, \tag{6}$$

where $\Gamma(\alpha)$ is the Gamma function, and κ_η is the modified Bessel function of the second kind of order η. The inverse timescale parameter, $h > 0$, For $\omega \gg h$, the process exhibits power-law decay, whereas for $h \to \infty$, or equivalently for $\omega \to 0$, the process behaves like a white noise process, as could be expected if we were to observe Lagrangian velocities sparsely over long very time intervals. The Matérn process provides a continuum between these two regimes over different timescales, controlled by the value of h, which has the units of an inverse timescale parameter. The slope parameter, $\alpha > 1/2$, controls the degree of smoothness or differentiability of the process. The Matérn process generalizes and unifies the various stochastic models for the turbulent background proposed in the previous oceanographic literature.

Combining the above two models for the inertial oscillation and turbulent background process to form an aggregated statistical model for drifter velocity time series, characterized by the spectrum

$$S(\omega;\theta) = \frac{A^2}{(\omega-\omega_f)^2+c^2} + \frac{B^2}{(\omega^2+h^2)^\alpha}, \tag{7}$$

where $\theta = (A, B, \omega_f, c, h, \alpha)$ is an array of model parameters.$S(\omega;\theta)$ is, therefore, a six-parameter model: ω_f, $c > 0$, and $A > 0$, respectively, correspond to the frequency, damping and amplitude of the inertial oscillation, and $B > 0$, $\alpha > 1/2$, and $h > 0$, respectively, correspond to the amplitude, smoothness, and timescale parameter of the turbulent background process.

The array of model parameters in formula (5) is estimated in the frequency domain. Conventionally, frequency-domain Whittle likelihood estimation is used to obtain the model parameters based on periodogram $\widehat{S}_Z(\omega)$. It is well known, however, that the periodogram is a poor estimator for the spectral density. In order to obtain better parameter estimation accuracy, the blurred Whittle likelihood is approached following (Sykulski et al. 2015):

$$l_b(\theta) = -\sum_{\omega\in\Omega}\left[\frac{\widehat{S}_Z(\omega)}{\overline{S}(\omega;\theta)} + \log\left\{\overline{S}(\omega;\theta)\right\}\right], \tag{8}$$

where periodogram $\widehat{S}_Z(\omega)$ is calculated using the Fourier transform of the time series Z(t), i.e. $\widehat{S}_Z(\omega) = \frac{\Delta}{N}\left|\sum_{t=1}^{N}(Z_t - \overline{Z})\exp(-it\omega\Delta)\right|^2$, the N is length of time series, Δ is the sampling interval, the $\overline{Z} = \sum_{t=1}^{N} z_t/N$ is sample mean, ω is Fourier frequency. The expected periodogram $\overline{S}(\omega;\theta)$ is conveniently given in terms of the true autocovariance function, i.e., $\overline{S}(\omega;\theta) = \Delta\sum_{\tau=-(N-1)}^{N-1}\left(1-\frac{\tau}{N}\right)s_\tau(\theta)\exp(-i\tau\omega\Delta)$, where the autocovariance function $s_\tau(\theta)$ is the sum of the autocovariance sequences given in equations given in (3) and (5). The best-fit parameters $\widehat{\theta}$ is obtained by maximizing the blurred likelihood function $l_b(\theta)$.

In summary, the LSM shows the significant advantages comparing with previous models. (1) The mode consistently captures ocean variability by aggregating two simple stochastic processes from drifter trajectories. (2)This model allows parameters to be estimated locally in time using short windows, yielding parameter estimates with high temporal and spatial resolution. (3) The stochastic model is the first to explicitly include the effects of inertial oscillations. (4) The turbulent background modeled by the Matérn process flexibly accounts for the various spectral slopes observed in the real data.

3 Results

3.1 Estimates of mean flow and eddy kinetic energy

When analyzing Lagrangian data, generally the first task is to estimate the mean flow accurately. In previous works, the mean flow was estimated using either the Eulerian or Lagrangian framework. As the best way to estimate a Lagrangian-based mean field remains an unsolved question, the Eulerian-based estimate was used for the mean flow in this study. Following Veneziani et al. (2004), the bin averaging and spline interpolation techniques were used to estimate the mean flow of the northern SCS and Northwest Pacific. The caveat was that the average was performed over a complete dataset in seasonal terms because of insufficient data to resolve non-stationarity. The drifter velocities were interpolated and then averaged over spatial bins and a certain period (Poulain and Niiler 1989). An array bias will affect mean flow estimates when the sampling array is not uniform. The effects of nonuniform sampling make it difficult to piece together an accurate description of the general circulation from floats deployed in localized regional arrays, it can be partially corrected by computing the Lagrangian diffusivity (Davis 1991). In present work, some experiments are performed by changing the bin size to test the sensitivity of the results to minimize the array bias.

The mean flow displays the strong Kuroshio system, with mean velocities of $1.8\text{m}\cdot\text{s}^{-1}$ in the east of Taiwan island. The north equatorial current splits into two branches at 5°N, with the northern branch moving into the Kuroshio along eastern Philippines. After moving northward to Japan, a branch of the Kuroshio turns southward to form a distinct and giant eddy with its center located near 135°E, 30°N. There is a cyclonic circulation in the northwest area of Luzon Island, with its center located near 118°E, 17.5°N, called the Luzon cold eddy. On the southeast side of the circulation, a coastal current coming from the middle of the SCS moves northward along the west coast of Luzon Island, namely the Luzon coastal current, with a maximum velocity exceeding $0.9\text{m}\cdot\text{s}^{-1}$ in summer. The associated intrusion of the Kuroshio into the SCS via Luzon strait will be discussed in Sect. 3.2. The mean flow of the northern SCS is closely related to seasonal reversals in the prevailing current because of the monsoon (Qian et al. 2013). The southwest monsoon prevails in summer, an anticyclone controls the northern SCS, and the northward current dominates the Taiwan Strait. In winter, the SCS is dominated by the northeast monsoon, the northern SCS is a cyclone, and the southward current dominates the Taiwan Strait. A few errors were observed in the mean flow estimates. The error sources included measurement errors, inaccuracies associated with the velocities computed from the drifter locations, and sampling errors related to the finite dataset.

Eddy kinetic energy (EKE) is one of the usable forms of energy in the oceans. According to Poulain (2001), in Eulerian statistics, EKE is defined as $\text{EKE} = u'^2 + v'^2/2$ under the assumptions of geostrophic balance and isotropy. The zonal component u' and meridional component v' are computed as $u' = u(t) - \overline{u}$ and $u' = v(t) - \overline{v}$,where $\overline{u}, \overline{v}$ are averaged over small spatial bins and over a certain period (Qian

et al. 2013; Veneziani et al. 2004). We have computed the seasonal mean eddy kinetic energy (mEKE), i.e., $\mathrm{EkE_m} = \left(\overline{u\prime^2} + \overline{v\prime^2}\right)/2$, and shown in Fig. 3. The largest EKE values were calculated for the Luzon Strait and the northeastern part of Taiwan Island ($1600\mathrm{cm}^2 \cdot \mathrm{s}^{-2}$), which are similar to the estimated EKE pattern based on altimetry data (Cheng and Qi 2010; Nan et al. 2015). The region east of the Kuroshio axis in the Luzon Strait has a high probability of eddy occurrence (> 30%) (Qian et al. 2013), and is characterized by high EKE. The EKE estimated by the drifter is affected not only by mesoscale variability and turbulent energy, but also by various factors such as the seasonal cycle and low-frequency variability.

3.2 Kuroshio intrusion

The Luzon Strait is an important passage connecting the Philippine Sea with the SCS. The Kuroshio passing through the Luzon Strait causes a series of dynamic and kinematic changes owing to the loss of continental slope support. According to Nan et al. (Nan et al. 2011, 2015), there are different views on how the Kuroshio intrudes into the SCS, whether in the form of looping path, leaping path, or leaking eddies (Hu et al. 2000).Although multiple flow patterns for the Kuroshio intrusion have been descriptive and schematic, how to define an index to distinguish different types of Kuroshio intrusion quantitatively is significantly important to understand the Kuroshio intruding processes and dynamics (Nan et al. 2015). The index should be derived based on readily available observations or credible ocean model output.

Figure 4a contains a total of 41 drifters entering the SCS along two paths, mainly including leaking path and looping path, while Fig. 4b shows the leaping path drifters with a total of 37. The leaking path is the most frequent from with the probability of occurrence at 75.61%, while the probability of occurrence the looping path is 24.39%, which is consistent with the result of Yuan et al. (2006). The proportion of the leaking and looping paths is defined as the intrusion coefficient, namely 0.52, which is slightly smaller than the Nan et al. (2015), considering the insufficient number of drifters.

The Kuroshio flows northward along the eastern coast of the Luzon Strait and Taiwan, and then the northward-flowing Kuroshio bifurcates when it collides with the zonally running shelf break of the ESC defined by the 200 m isobath (Wu et al. 2015). Because of the loss of the supporting role of Taiwan Island, the Kuroshio turns in the northeast sea of

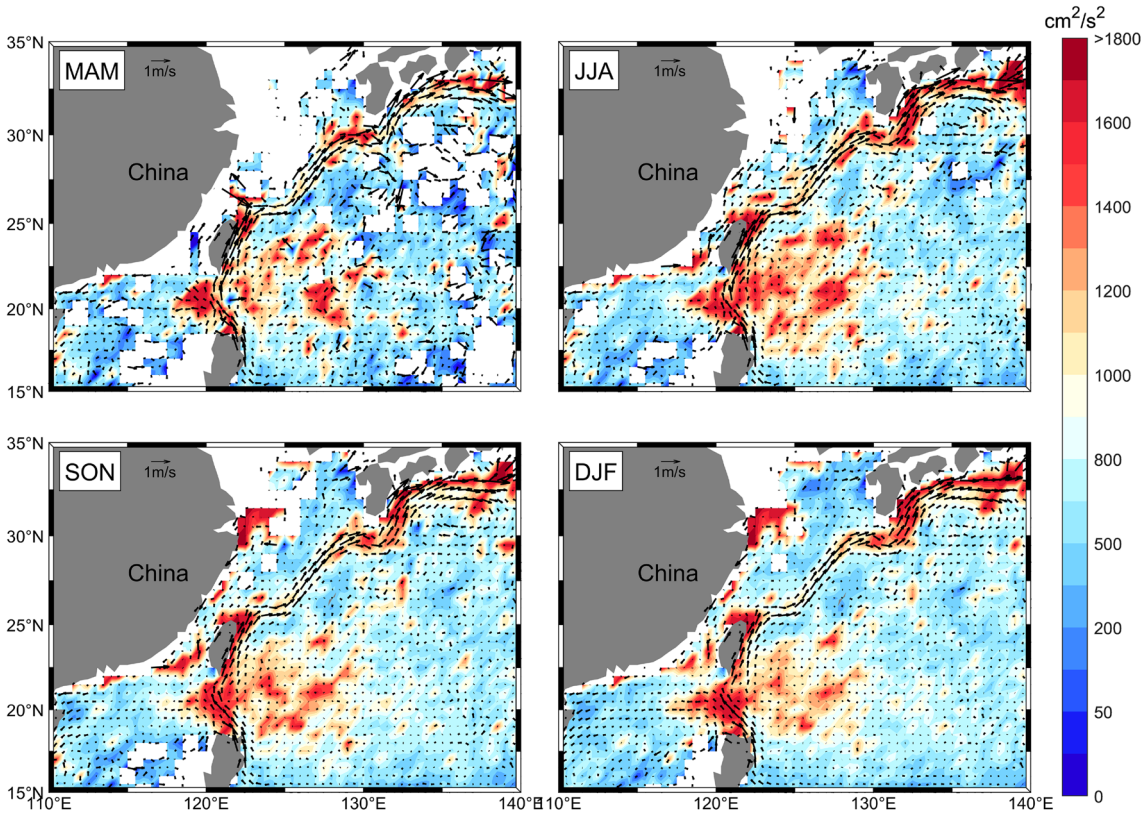

Fig. 3 Pseudo-Eulerian mean velocity field and mean EKE in 0.5° bins during spring (MAM), summer (JJA), autumn (SON), and winter (DJF)

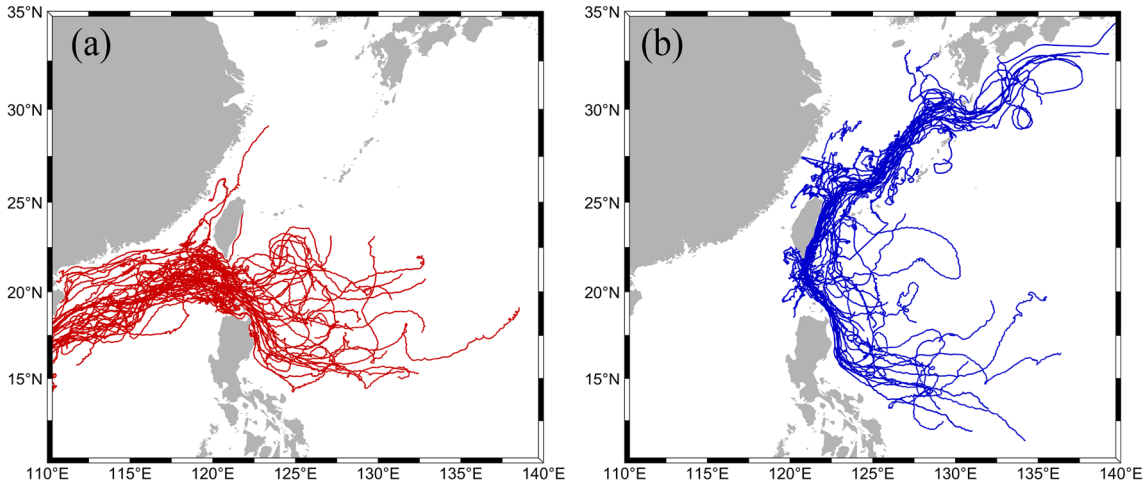

Fig. 4 Drifter trajectories, **a** red trajectories indicate drifters entering the South China Sea with leaking path and looping path, **b** blue trajectories indicate drifters along the Kuroshio and intruding the East China Sea with leaping path

Taiwan and then invades the ECS shelf (Liu et al. 2015). The details of this process are not of concern in this study.

3.3 LSM application on a GDP drifter

As a first step, we first apply LSM to a 401-day (August 20, 2009–September 26, 2010) trajectory of a Northwest Pacific Ocean drifter, with GDP ID #71,153, shown in Fig. 5a. We apply a relatively long window length of 2400 time points, corresponding to a 100 days trajectory indicative of green line in Fig. 5a. This is because we have deliberately reduced variance, at the expense of bias, for this single drifter analysis. Figure 5b displays rotary spectrum of the observed (black solid and dashed line) and modeled (red line) log-spectra for velocity time series recorded by the 100-day trajectory. We see that the six parameters model appears to accurately capture the spectral structure over the modeled band of frequencies. The model identifies the inertial frequency shift as occurring at the local Coriolis frequency. According to Kunze (1985), the inertial frequency will be modified under the condition of background current, resulting the effective Coriolis frequency, i.e., $f_{\text{eff}}{}^2 = \left(f^2 + f\frac{\partial v}{\partial x} - f\frac{\partial u}{\partial y} - \frac{\partial u}{\partial y}\frac{\partial v}{\partial x} + \frac{\partial u}{\partial x}\frac{\partial v}{\partial y}\right)$. The observed frequency-shifting of the inertial peak mainly is due to eddy variability, which is captured by LSM. The model fit parameter shows the amplitude (A) and damping (c) of the inertial oscillation is 3.73 and 0.029, respectively. Thus, the corresponding amplitude and damping e-folding time scale of inertial current is 3.73 cm $\cdot$ s^{-1} and 9 days. The amplitude, slope (smoothness) and time scale parameter of turbulent background given by model is 0.20, 1.75 and 0.002, respectively, and shows the mesoscale background motions is weak flowing the trajectory of the drifter, which is consistent with weak eddy kinetic energy far away the Kuroshio edge. The slope parameter governs the aspect ratio of rescaling for self-similar behavior, i.e., when we "zoom in" in time to observation, the greater the slope parameter value, the weaker the self-similar behavior. The large slope parameter value 1.75 imply the motion hold weak self-similar. The damping parameter $h = 0.002$ of geostrophic is indicated in Fig. 5b, which is a breakpoint between a low-frequency plateau and a high-frequency slop.

The time-varying parameters are estimated by considering a rolling window of observations from the overall time series. In order to produce accurate time-varying estimation of the model parameters, choice of window length is important, so that the model parameters vary little over the window timescale, while the window is still large enough to reduce variance of the parameter estimates. Longer windows will decrease the variance but simultaneously increase bias, and shorter windows may miss a few features (Guillaumin et al. 2017). The determination of window length is empirical. To resolve spatial heterogeneity at small and large scales in the oceans, high spatial resolution parameter output is needed, so the use of shorter windows will be favored as recommended by Sykulski et al. (2016), when multiple trajectories are available within a given spatial region. Bias can then be reduced, and the variance is instead reduced by averaging over the multiple time series.

Time-varying spectra of GDP ID#71,153 display in Fig. 5 is shown in Fig. 6, resulting from a rolling-window fit with a window length 600 time points (or 25 days). During most of the time series, the model identifies the inertial frequency as occurring at the local Coriolis frequency shown as the black line; note that smooth variation of the estimated inertial frequency is observed. Generally speaking, the LSM captures the temporal variability observed in the moving-window

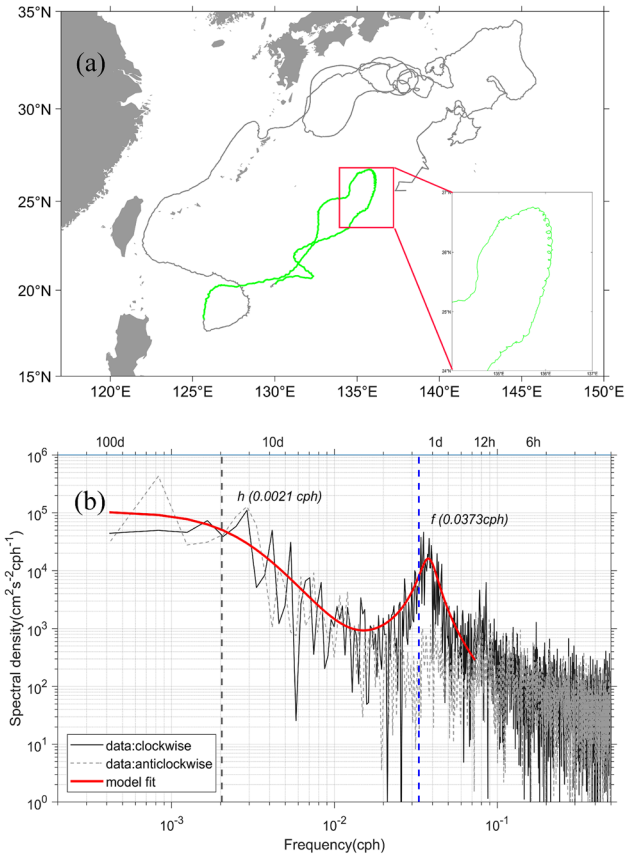

Fig. 5 **a** Black line shows 401-day (August 20, 2009–September 26, 2010) trajectory of the drifter ID #71,153. Green line indicates the 2,400 time points, corresponding to a 100 days trajectory are analyzed. The zoom in portion shows significant inertial oscillation signal. **b** Rotary spectrum of green trajectory and LSM fit. The solid (dashed) black line is clockwise (anticlockwise) spectra. The fitted spectra in the inertial and turbulent background frequency band by LSM are shown in red solid lines. The local (25.972°N) inertial frequency f and damping parameter of geostrophic turbulence h is labeled using vertical dashed line.)

periodogram at both the inertial peak and the low-frequency peak, and this good agreement shows that structure in the data can be well accounted for using the LSM.

Figure 7 shows the estimates of the six time-varying parameters using LSM, which evolve over time relatively smoothly. The inertial oscillation is shown to significantly shift from the theoretical frequency particularly between days 0–100 and days 200–350. Inspecting Fig. 7 in more detail, we can see that there is a high band of energy during this time period near the Coriolis frequency. The strongest inertial energy band present in the days 200–350, where the fitted parameter shows strong inertial oscillation amplitude (Fig. 7b) and a long damping timescale appears (Fig. 7c) in the days 200–350. During the days 0–120, original spectrum also shows high energy in the inertial frequency band, but the amplitude of NIO recovered by LSM relatively hold small value, comparing with the days 200–350. In fact, the fitted high energy spectrum is determined by low amplitude and large damping parameter (corresponding short damping timescale).

There is a stronger energy at the low-frequency band in the days 150–300 as shown in the original spectrum (Fig. 6), LSM also correctly captures the spectrum structure. As shown in Fig. 7, the fitted LSM holds large amplitude parameter B with relatively small slope and smooth parameter. The drifter was caught in the strong Kuroshio current and interned into the central axis of the Kuroshio from days 120 to days 160. The near-inertial energy is weak, and corresponding fitted inertial oscillation amplitude and damping parameter rapidly decreases during the period.

3.4 Spatial characteristic of NIOs

Previous studies in this region have frequently focused on NIOs motivated by simple cyclones. Chen et al. (2015) found that a solid NIOs is triggered when a cyclone front passes over the sea surface, which can last for 1 ~ 2 weeks, with the maximum value reaching 0.5 ~ 1m·s^{-1}.

Firstly, we can observe the shifting of inertial oscillation frequency, mainly due to the influence of background eddies (Fig. 3). In the cyclone region, the effective Coriolis frequency is larger than the local Coriolis frequency because of the existing positive vorticity, conversely, the effective Coriolis frequency is smaller than the local Coriolis frequency due to the negative vorticity. In order to investigate the shifting of inertial oscillation frequency, the relative frequency shift (RFS) was defined as:

$$RFS = \frac{\omega_f - f}{f}, \tag{9}$$

where f is the local inertial frequency of the mean latitude of the corresponding 25-d trajectory, ω_f is the spectral peak frequency. A positive (negative) RFS means that the observed frequency is higher (lower) than theoretical Coriolis frequency f, namely blue (red) shift occurring. Inspecting the spatial distribution of the RFS (Fig. 8), the blue shift predominates the northern SCS, Luzon strait, and Philippine Sea, and the red shift dominates the areas of Kuroshio extension. The blue shift in the northern SCS and the Luzon Strait may have been influenced by the storm (Alford et al. 2016). The blue shift also is interpreted in the context of the generation and propagation of near-inertial motion at the scale of the ocean basin, i.e., NIOs are free to propagate toward the equator and therefore will always have a frequency higher than the local inertial frequency. In addition, phenomenon of blue shift in NIOs is also related to its damping effect (Fu 1981; Garrett 2001).

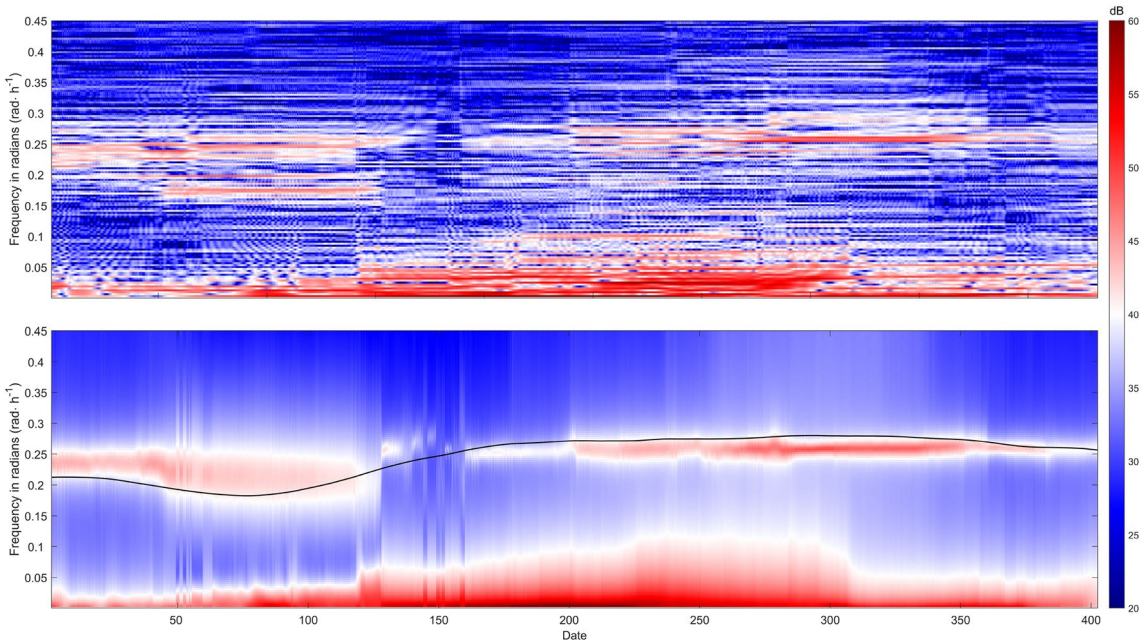

Fig. 6 Time-varying spectra of the drifter ID#71,153 display in Fig. 5, where red and blue denote high and low energy, respectively. **a** The spectrum of observed data; **b** modeled spectrum using LSM. Black curve indicates the local inertial frequency)

Figure 9 shows the spatial variation of amplitude and decay timescale of near-inertial oscillation. The amplitude reflects the strength of the NIOs. It is visible that the Luzon strait has a predominance of high amplitudes. The amplitude is lower in the north Philippine Sea than that in the south, where the Kuroshio overflows from low latitudes to the SCS via the Luzon Strait. The amplitude of inertial oscillation along the Kuroshio path in northern Guam is significantly lower than that in other regions. The reciprocal of damping parameter given by LSM is a measure of time scale of NIOs, which is shown in Fig. 9b. The low values (around 2.7 day) of damping timescale appear in the northern SCS and Philippine Sea, where the amplitude of NIOs holds relatively large values (Fig. 9a), and blue shift of NIO frequency occurs (Fig. 8). Elipot et al. (2010) demonstrated that there was a positive linearly correlation between NIV and its decay time scale from a global perspective. If the damping timescale is short, and the inertial energy decay rapidly, and corresponding NIV is weak. Conversely, NIV will increase with extension of its decay period. NIOs are observed to have larger variance when they are of longer time scales, which implies more persistent time according to Fu's (1981) interpretation. The near-inertial frequency shift caused by strong positive vorticity in this region results the speeding up of the NIOs. Long damping timescale for NIOs mainly occurs in the norther to 25°N in the study area, where the anticyclonic eddies are active, accompanied by red shift of NIOs (Fig. 8). The NIOs frequency shift caused by the positive vorticity will accelerate the decay period of the near-inertial motion (Elipot et al. 2010). Which may be responsible for the energy transferring from geostrophic flow to near-inertial motions (Jing et al. 2017).

To better understand the energy of NIOs, the regional spatial distribution of the NIV is calculated. NIV is defined the integral of kinetic energy in near-inertial peak (Elipot et al. 2010), i.e.,

$$NIV = \int_{\Delta\omega} S(\omega) d\omega, \tag{10}$$

where $\Delta\omega$ is inertial frequency band, various inertial frequency bands have been used in previous studies. Pall et al. used a frequency band range of $0.9 - 1.15f$ to study NIOs in the Gulf (Pallàs-Sanz et al. 2016). Hou (2019) used $0.7 - 1.2f$ in the Northwest Pacific. In the study, we selected an adaptive frequency window, which is considered as half power of the peak. The spatial distribution of the NIV is present in Fig. 10a. In general, the spatial pattern of NIV is similar with that of NIOs amplitude as shown in Fig. 9a. High NIV values were observed in the northern SCS and Luzon Strait, where the near-inertial motion is active (Guo et al. 2020), while the lowest NIV presents in the mainstream of the Kuroshio. The peak NIV values (approximately $350\text{cm}^2 \cdot \text{s}^{-2}$) appeared in the northwest of Luzon Island.

Wind stress fluctuations in the near-inertial band can resonantly force near-inertial oscillations in the surface mixed layer (Alford et al. 2016). Figure 10b shows the synchronous

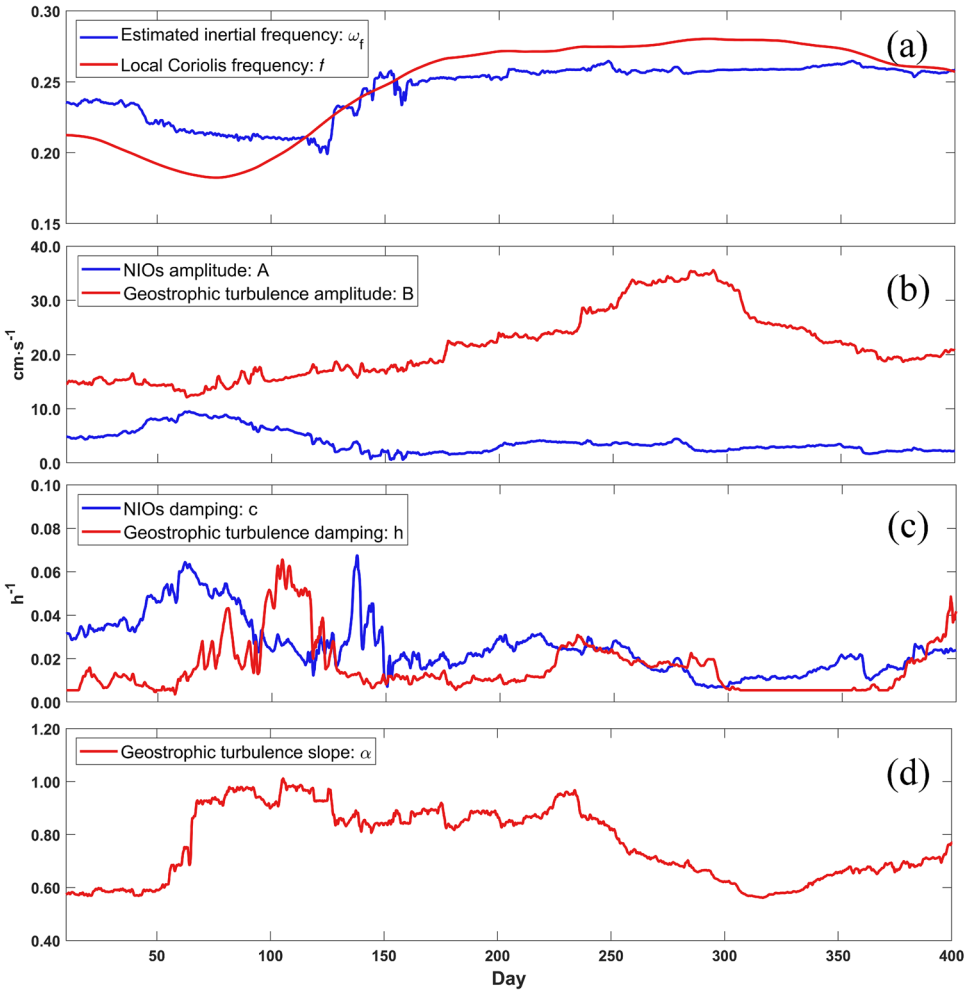

Fig. 7 Time-varying parameter values of the model fits of Fig. 6: **a** estimated inertial frequency and local Coriolis frequency; **b** amplitude of NIOs and geostrophic turbulence; **c** damping of NIOs and geostrophic turbulence; **d** slope of geostrophic turbulence

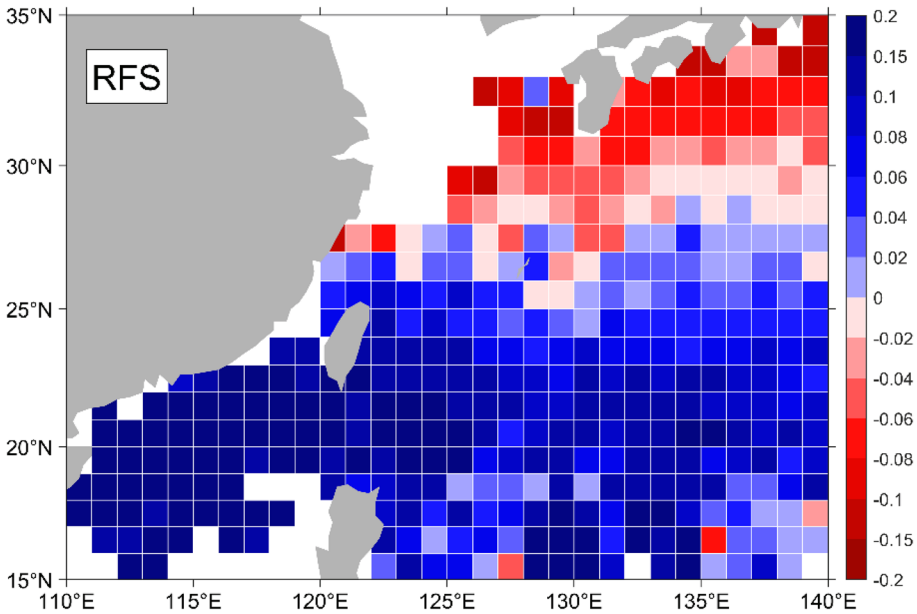

Fig. 8 spatial distribution of relative frequency shift for NIOs

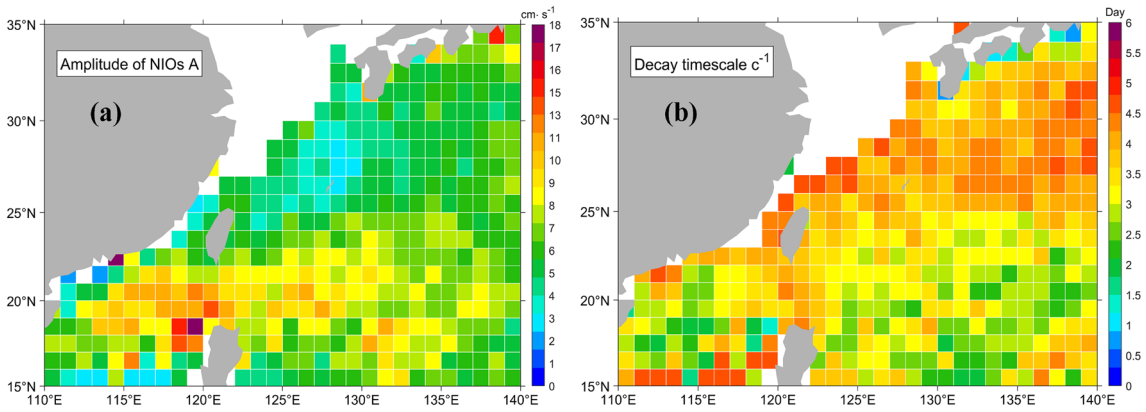

Fig. 9 The spatial distribution of amplitude **a** and decay timescale **b** of NIOs

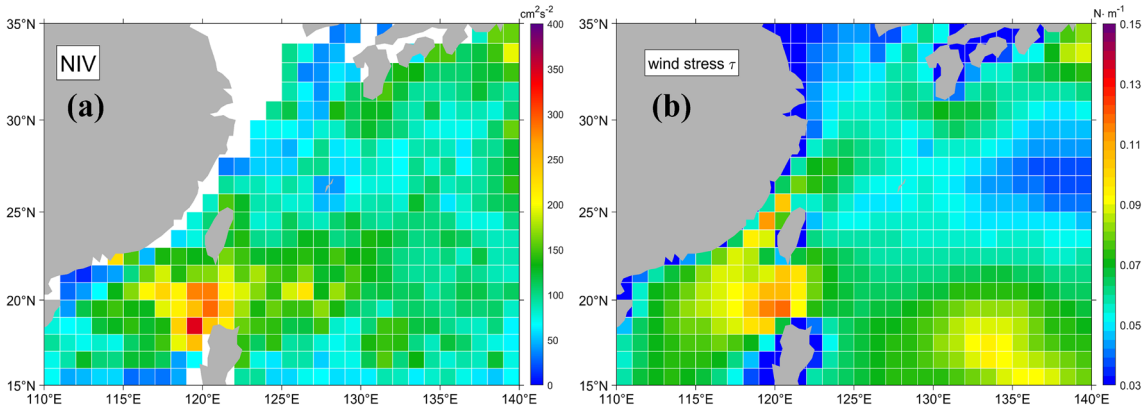

Fig. 10 The spatial distribution of near-inertial variance **a** and wind stress **b**

wind stress with drifter observation from ERA5 dataset, which is used to discuss the relation between the distribution of inertial current amplitude and wind fluctuation. Here the wind stress is computed as $\boldsymbol{\tau} = \rho_a C_D |\boldsymbol{U}_{10}| \boldsymbol{U}_{10}$ according to Liu et al. (2019), where ρ_a is the air density approximated as a constant of 1.22 kg · m^{-3}, C_D is the drag coefficient, $\boldsymbol{U}_{10}$ is the wind vector at 10 m. According to Large and Pond (1981), the value of drag coefficient is given as

$$C_D = \begin{cases} 1.2 \times 10^3 & U_{10} \ll 11\text{m} \cdot \text{s}^{-1} \\ (0.49 + 0.065U_{10}) \times 10^3 & U_{10} \gg 11\text{m} \cdot \text{s}^{-1} \end{cases}.$$

The pattern of NIV of NIOs is similar with the strength of wind fluctuation, and the strongest NIV present in the Luzon strait and northern SCS, where the wind fluctuation also shows strongest.

3.5 Spatial characteristic of geostrophic turbulence

In the LSM, the low-frequency parts below inertial period from the Lagrangian velocity time series is fitted by Matérn process, which simultaneously capture the effects of long-timescale diffusivity and small-scale fractal dimensionality(Lilly et al. 2017). The best-fit values of the three Matérn parameters (B, α, h) allows us to simultaneously vary the values of the three most important properties of Lagrangian trajectories: the kinetic energy, the degree of small-scale roughness and long-time diffusive behavior. Matérn process is demonstrated to show an excellent match for Lagrangian velocity spectra for two-dimensional turbulence (Lilly et al. 2017). It is known that the zero-frequency value of velocity spectrum quantifies the dispersive tendency, and a primary characteristic of Lagrangian trajectories is their tendency to diffuse at a uniform rate at long times (Koszalka and LaCasce 2010; LaCasce 2008).

In Matérn parameters, α present the slope parameter, and with B setting the spectral level. Velocity spectrum from Lagrangian trajectories are found to exhibit power-law behaviors at high frequencies (Rupolo et al. 1996). For a range of spectral slopes, the power-law spectrum corresponds to that of a Gaussian random process called fractional Brownian motion, which is a generation of classical

Brownian motion – corresponding to the case $c = -1$ and, therefore, to an ω^{-2} spectrum. The variance and the diffusivity of fractional Brownian motion, where damping parameter h is not involved, will be found to increase without bound. The decrease in the degree of roughness as α increase, and the spectral slope becomes steeper. This occurs since higher values of α correspond to stronger degrees of "filtering", with steep spectral slopes removing high-frequency contributions to variance.

Figure 11 shows spatial distribution of the amplitude, decay timescale of the geostrophic turbulent fitted by LSM. The large geostrophic turbulent amplitude is along the Kuroshio path, and maximum value reach to 30cm $\cdot$ s^{-1}. The mesoscale eddies are usually active on both sides of the western boundary current Kuroshio due to the shear instability. In the inner region far away boundary current, the geostrophic turbulent is weak with small amplitude parameter obtained by LSM.

Damping parameter h is inverse timescale, which measures the diffusion property of the background turbulence. Low-frequency motion with a frequency lower than h is often resembled as white noise. For a more convenient understanding, Fig. 11b shows the distribution of reciprocal of damping parameter h, namely decorrelation timescale, which also is a breakpoint between a low-frequency plateau and a high-frequency slop. The decorrelation timescale in the northern SCS is lower than that in the Philippine Sea. A higher damping parameter h corresponds to a lower decorrelation timescale, and such motion is more approaching to white noise.

The slope parameter, $\alpha > 0.5$, controls the degree of smoothness or differentiability (Gneiting et al.2012), which is shown in Fig. 12a. High slope parameters predominate in the northern SCS and exhibit an extreme value of greater than 1.5. High values are also dominant in the area from the Luzon Strait to the Philippine Sea, where the amplitude is lower than others. The isotropic diffusivity κ, which quantifies the expected rate at which the particles disperse, or spread out, over time from an initial location, is related to the parameters of Matérn process. The diffusivity is defined as the zero-frequency value of velocity spectrum. According Eq. (6), $\kappa(t) = \frac{B^2(t)}{4\left(h^2(t)\right)^{\alpha(t)}}$. For a given Lagrangian velocity

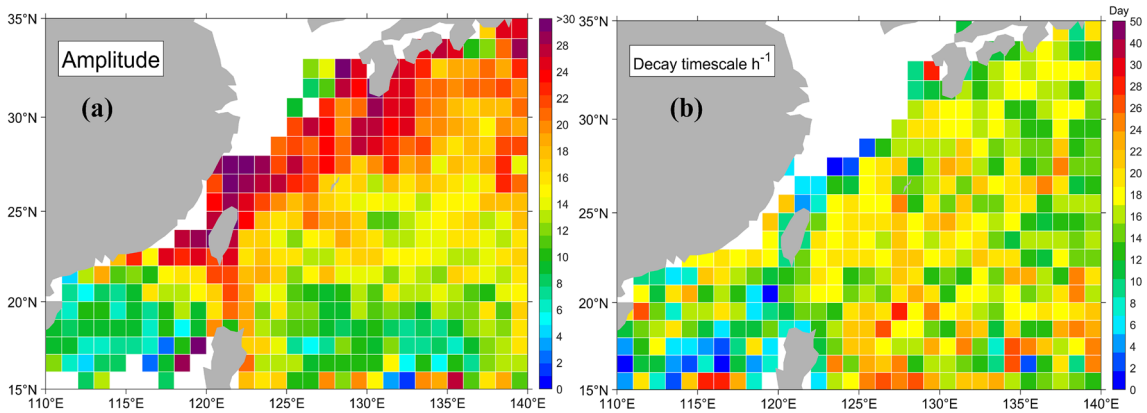

Fig. 11 Spatial distribution of amplitude **a**, damping timescale **b** of geostrophic turbulence

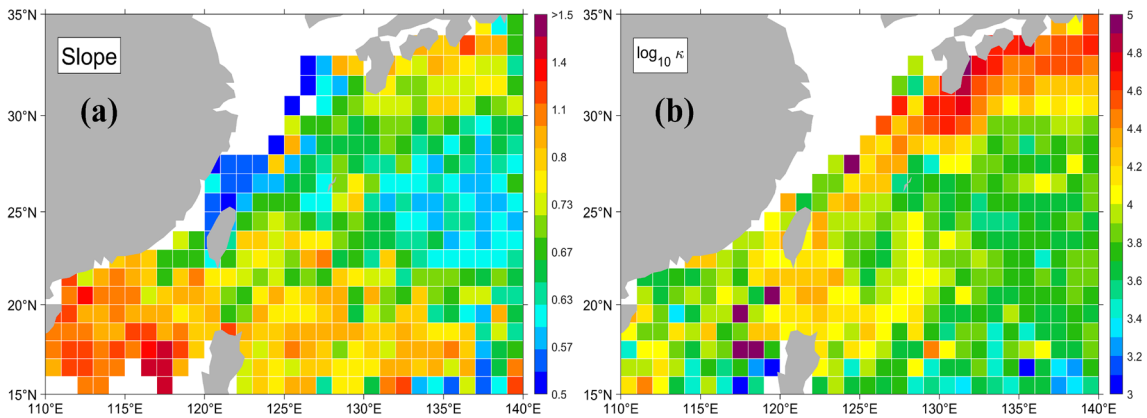

Fig. 12 Spatial distribution of slope parameter **a** and isotropic diffusivity κ **b** of geostrophic turbulence

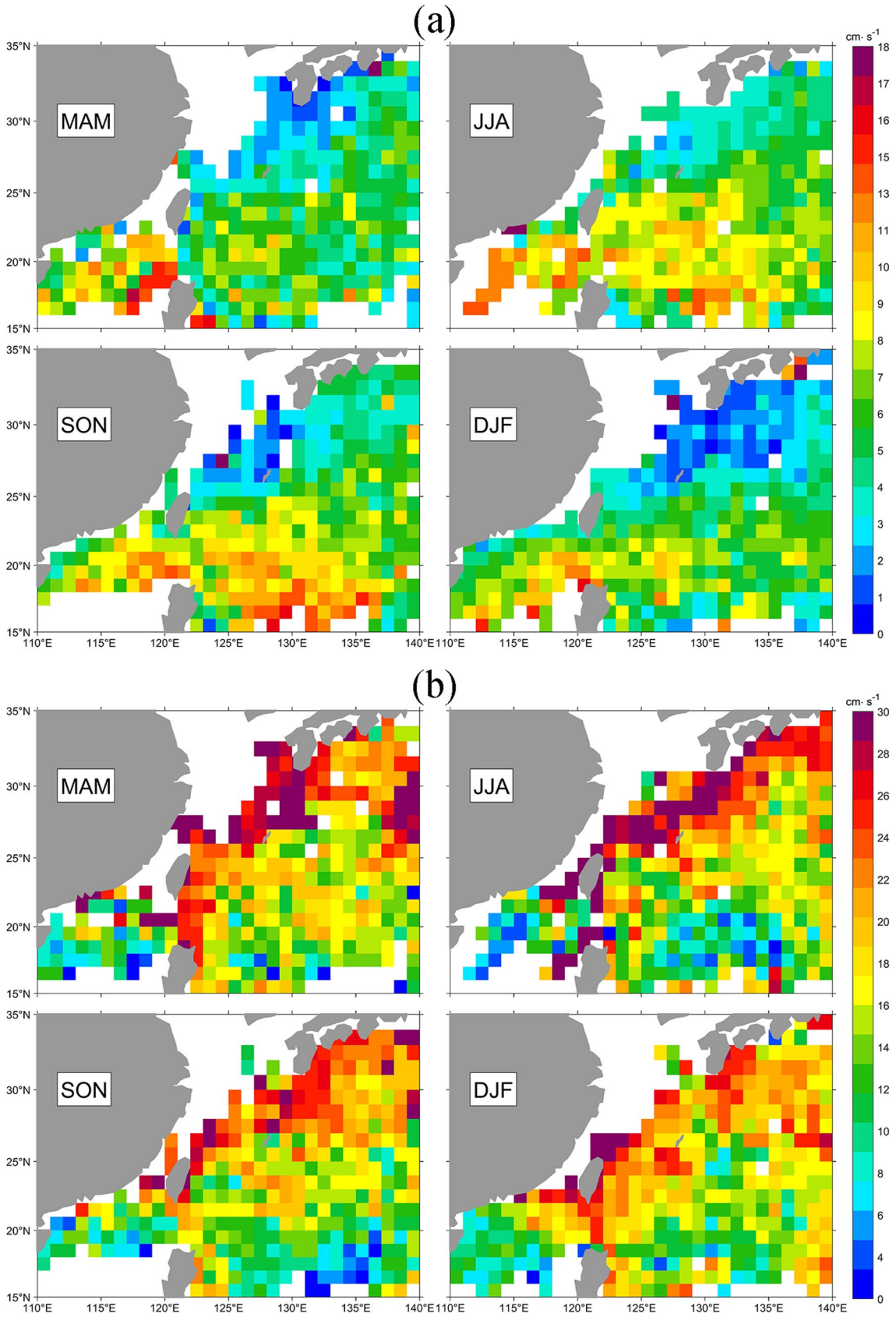

Fig. 13 Distribution of the NIOs amplitude **a** and geostrophic turbulence amplitude **b** during spring (MAM), summer (JJA), autumn (SON) and winter (DJF)

time series $z(t)$, we will refer to $z(t)$ as a diffusive process if it is associated in this way with a non-zero and finite value of κ. Processes associated with zero values of κ will be said to be sub-diffusive, while those associated with unbounded values of κ will be referred to as super-diffusive. Figure 12b gives the distribution of diffusivity k. The isotropic diffusivity is higher along the Kuroshio path, which is consistent with the high geostrophic turbulent. Thus, the geostrophic turbulence region with stronger amplitude is usually accompanied by higher isotropic diffusivity.

3.6 Seasonal variation of NIOs and geostrophic turbulence

The seasonal averaged amplitude is illustrated in Fig. 13. Although spatial structures persisted, the magnitudes of these parameters varied with time. The amplitude of NIOs exhibits seasonal variations based on the velocity data recorded by moored current-meter in the northern SCS (Chen et al. 2013). In addition, there is a striking contrast in the number of observations between summer and winter. The intense summer monsoon is vital for generating strong NIOs (Shu et al. 2016).

The seasonal variation in the NIOs amplitudes, presented in Fig. 13a, is regionally asynchronous. The amplitude of NIOs in the northern SCS is higher than that in other areas all year. The amplitude peak occurs in autumn in the Philippine Sea and in summer in the Kuroshio region. During winter monsoon, a significant value region extends from the Luzon Strait with a northeast-to-southwest trend. The NIOs amplitude in summer is overall 15–20% higher than that in winter. The amplitudes of geostrophic turbulence depicted in Fig. 13b display no considerable seasonal variation, and the weakest value in the Kuroshio region appears in winter. The stable spatial distribution shows that the amplitude is stable in time and less affected by seasonal variation.

4 Conclusions

This study investigated the inertial oscillation and background current by fitting the complex velocity spectrum of Lagrangian time series derived from Global Drifter Program datasets with a new stochastic model developed by Sykulski et al. (2016), which combines the Complex-valued Ornstein–Uhlenbeck and Matérn stochastic processes. The OU stochastic process captures inertial oscillation characteristics of the velocity time series, while the Matérn process can describe the geostrophic turbulent background spectrum. We extracted six ocean dynamics parameters and analyzed the temporal and spatial variability.

Mean flow derived from the drifters clearly demonstrates the strong Kuroshio system and monsoon circulation over the northern SCS, which includes the Kuroshio intrusion at the Luzon Strait. The Luzon Strait and its eastern part exhibit high EKE and near-inertial variance, with the eastern part displaying a high probability of eddy occurrence. The complex circulation system and background vorticity exerts the influence the near-inertial motions.

The effect of background vorticity on inertial frequency shift is significant; when the low-frequency background is cyclone, the near-inertial frequency increases (blue shift), and vice versa (Alford et al. 2016). The NIOs frequency shift caused by the positive vorticity will shorten the decay period of the near-inertial motion. The NIOs amplitude is different at different latitudes, the Kuroshio has lower amplitude in the north, and the near Luzon Strait has an extensive range of amplitudes related to the vigorous cyclone activity here. The stronger geostrophic turbulence appears in the mainstream of Kuroshio and its extension. The geostrophic turbulence has a highly significant effect in the Kuroshio, whereas the NIOs play the dominant role in the Luzon Strait and northern SCS. In terms of seasonal mean, although spatial structures persisted, the magnitudes of these parameters varied with time. The amplitude of NIOs in summer is higher than in winter and is greater in the region with weak geostrophic turbulence.

The fit of NIOs by the stochastic model is time dependent; therefore, the stationarity of the drifter velocity spectrum assumed in our analysis is not always true (Guillaumin et al. 2017). However, the compatibility of our observations with analytical and numerical predictions suggests that these theories may at least be partly applicable to the actual ocean.

Acknowledgements The authors are grateful to anonymous reviewers for their instructive review. The altimeter products were provided by Copernicus Marine Environment Monitoring Service (CMEMS, http://marine.copernicus.eu/services-portfolio/access-to-products/). The drifter data were provided by Global Drifter Program (GDP, https://www.aoml.noaa.gov/phod/gdp/data.php). The code for the stochastic modeling of Lagrangian trajectories was provided by Sykulski (www.ucl.ac.uk/statistics/research/spg/software). This study was supported by the National Nature Science Foundation of China (Grant No.42076015).

Data availability All data availblity used in the paper is have mentioned in the acknowledgement.

References

Alford MH, MacKinnon JA, Simmons HL, Nash JD (2016) Near-inertial internal gravity waves in the ocean. Ann Rev Mar Sci 81(1):95–123. https://doi.org/10.1146/annurev-marine-010814-015746

Berloff PS, McWilliams JC (2002) Material transport in oceanic gyres .Part ii: hierarchy of stochastic models. J Phys Oceanogr 32(3):797–830. https://doi.org/10.1175/1520-0485(2002)032

Chaigneau A, Pizarro O, Rojas W (2008) Global climatology of near-inertial current characteristics from lagrangian observations. Geophys Res Lett. https://doi.org/10.1029/2008gl034060

Chen GX, Xue HJ, Wang DX, Xie Q (2013) Observed near-inertial kinetic energy in the northwestern South China Sea. J Geophys Res Oceans 118(10):4965–4977. https://doi.org/10.1002/jgrc.20371

Chen S, Hu J, Polton JA (2015) Features of near-inertial motions observed on the northern South China Sea shelf during the passage of two typhoons. Acta Oceanol Sin 34(1):38–43. https://doi.org/10.1007/s13131-015-0594-y

Cheng XH, Qi YQ (2010) Variations of eddy kinetic energy in the South China Sea. J Oceanogr 66(1):85–94. https://doi.org/10.1007/s10872-010-0007-y

D'Asaro EA (1989) The decay of wind-forced mixed layer inertial oscillations due to the β effect. J Geophys Res. https://doi.org/10.1029/JC094iC02p02045

Davis RE (1991) Observing the general circulation with floats. Deep Sea Res I 38:S531–S571. https://doi.org/10.1016/s0198-0149(12)80023-9

Davis RA, Klüppelberg C, Steinkohl C (2013) Statistical inference for max-stable processes in space and time. J R Statist Soc B 75(5):791–819. https://doi.org/10.1111/rssb.12012

Elipot S, Lumpkin R, Prieto G (2010) Modification of inertial oscillations by the mesoscale eddy field. J Geophys Res. https://doi.org/10.1029/2009jc005679

Ferrari R, Wunsch C (2009) Ocean circulation kinetic energy: Reservoirs, sources, and sinks. Annu Rev Fluid Mech 41(1):253–282. https://doi.org/10.1146/annurev.fluid.40.111406.102139

Fu LL (1981) Observations and models of inertial waves in the deep ocean. Rev Geophys 19(1):141–170. https://doi.org/10.1029/rg019i001p00141

Garrett C (2001) What is the "near-inertial" band and why is it different from the rest of the internal wave spectrum? J Phys Oceanogr 31(4):962–971. https://doi.org/10.1175/1520-0485(2001)031

Gneiting T, Ševčíková H, Percival DB (2012) Estimators of fractal dimension: assessing the roughness of time series and spatial data. Statist Sci. https://doi.org/10.1214/11-sts370

Griffa A, Lumpkin R, Veneziani M (2008) Cyclonic and anticyclonic motion in the upper ocean. Geophys Res Lett. https://doi.org/10.1029/2007gl032100

Guillaumin AP, Sykulski AM, Olhede SC, Early JJ, Lilly JM (2017) Analysis of non-stationary modulated time series with applications to oceanographic surface flow measurements. J Time Ser Anal 38(5):668–710. https://doi.org/10.1111/jtsa.12244

Guinness J, Stein ML (2013) Interpolation of nonstationary high frequency spatial–temporal temperature data. Ann Appl Stat 7(3):1684–1708. https://doi.org/10.1214/13-AOAS633

Guo M, Chen R, Xu H, Vetter PA (2020) Dynamical features of near-inertial motions in global ocean based on the gdp dataset from 2000 to 2019. Acta Oceanol Sin. https://doi.org/10.1007/s13131-020-1675-0

Hou H (2019). Study on the nera-inertial wave in the northweat pacific (in Chinese). Dissertation, Insitute of OceanoLogy, Chinese Academic of Science

Hu J, Kawamura H, Hong H, Qi Y (2000) A review on the currents in the South China Sea: seasonal circulation, South China Sea warm current and kuroshio intrusion. J Oceanogr 56:607–624. https://doi.org/10.1023/A:1011117531252

Jing Z, Wu L, Ma X (2017) Energy exchange between the mesoscale oceanic eddies and wind-forced near-inertial oscillations. J Phys Oceanogr 47(3):721–733. https://doi.org/10.1175/jpo-d-16-0214.1

Koszalka IM, LaCasce JH (2010) Lagrangian analysis by clustering. Ocean Dyn 60:957–972. https://doi.org/10.1007/s10236-010-0306-2

Kunze E (1985) Near-inertial wave propagation in geostrophic shear. J Phys Oceanogr 15(5):544–565. https://doi.org/10.1175/1520-0485(1985)015

LaCasce JH (2008) Statistics from lagrangian observations. Prog Oceanogr 77(1):1–29. https://doi.org/10.1016/j.pocean.2008.02.002

Large WG, Pond S (1981) Open ocean momentum flux measurements in moderate to strong winds. J Phys Oceanogr 11(3):324–336. https://doi.org/10.1175/1520-0485(1981)011

Li J, Liu JL, Cai SQ, Pan JY (2015) The spatiotemporal variation of the wind-induced near-inertial energy flux in the mixed layer of the South China Sea. Acta Oceanol Sin 34(1):66–72. https://doi.org/10.1007/s13131-015-0597-8

Lilly JM, Sykulski AM, Early JJ, Olhede SC (2017) Fractional brownian motion, the matérn process, and stochastic modeling of turbulent dispersion. Nonlin Processes Geophys 24(3):481–514. https://doi.org/10.5194/npg-24-481-2017

Liu X, Chen D, Dong C, He H (2015) Variation of the kuroshio intrusion pathways northeast of taiwan using the lagrangian method. Sci China Earth Sci 59(2):268–280. https://doi.org/10.1007/s11430-015-5176-5

Liu Y, Jing Z, Wu L (2019) Wind power on oceanic near-inertial oscillations in the global ocean estimated from surface drifters. Geophys Res Lett 46(5):2647–2653. https://doi.org/10.1029/2018gl081712

Lumpkin R, Pazos M, Griffa A, Kirwan AD Jr, Mariano AJ, Ozgokmen T et al (2007) Measuring surface currents with surface velocity program drifters: the instrument, its data, and some recent results. Lagrangian analysis and prediction of coastal and ocean dynamics. Cambridge University Press, Miami, pp 39–67

Lumpkin R, Ozgokmen T, Centurioni L (2017) Advances in the application of surface drifters. Ann Rev Mar Sci 9:59–81. https://doi.org/10.1146/annurev-marine-010816-060641

Mooers CNK (1973) Several effects of a baroclinic current on the cross-stream propagation of inertial-internal waves. Geophys Fluid Dyn 6(3):277–284. https://doi.org/10.1080/03091927509365797

Munk W, Wunsch C (1998) Abyssal recipes ii: energetics of tidal and wind mixing. Deep Sea Res I 45(12):1977–2010. https://doi.org/10.1016/S0967-0637(98)00070-3

Nan F, Xue H, Fei C, Lei S, Shi M, Guo P (2011) Identification of different types of kuroshio intrusion into the South China Sea. Ocean Dyn 61(9):1291–1304. https://doi.org/10.1007/s10236-011-0426-3

Nan F, Xue HJ, Yu F (2015) Kuroshio intrusion into the South China Sea: a review. Prog Oceanogr 137(2015):314–333. https://doi.org/10.1016/j.pocean.2014.05.012

Pallàs-Sanz E, Candela J, Sheinbaum J, Ochoa J, Jouanno J (2016) Trapping of the near-inertial wave wakes of two consecutive hurricanes in the loop current. J Geophys Res Oceans 121(10):7431–7454. https://doi.org/10.1002/2015JC011592

Park JJ, Kim K, Crawford WR (2004) Inertial currents estimated from surface trajectories of argo floats. Geophys Res Lett. https://doi.org/10.1029/2004gl020191

Park JJ, Kim K, King BA (2005) Global statistics of inertial motions. Geophys Res Lett. https://doi.org/10.1029/2005gl023258

Park JJ, Kim K, Schmitt RW (2009) Global distribution of the decay timescale of mixed layer inertial motions observed by satellite-tracked drifters. J Geophys Res Oceans. https://doi.org/10.1029/2008jc005216

Pollard RT, Millard RC (1970) Comparison between observed and simulated wind-generated inertial oscillations. Deep-Sea Res 17(4):813–821. https://doi.org/10.1016/0011-7471(70)90043-4

Poulain PM (2001) Adriatic sea surface circulation as derived from drifter data between 1990 and 1999. J Mar Syst 29(1–4):3–32. https://doi.org/10.1016/S0924-7963(01)00007-0

Poulain PM, Niiler PP (1989) Statistical analysis of the surface circulation in the california current system using satellite-tracked drifters. J Phys Oceanogr 19(10):1588–1599. https://doi.org/10.1175/1520-0485(1989)019

Qian Y, Peng S, Li Y (2013) Eulerian and lagrangian statistics in the South China Sea as deduced from surface drifters. J Phys Oceanogr 43(4):726–743. https://doi.org/10.1175/jpo-d-12-0170.1

Rupolo V, Huang BL, Provenzale A (1996) Lagrangian velocity spectra at 700m in the western north atlantic. J Phys Oceanogr 26:1591–1607. https://doi.org/10.1175/1520-0485(1996)026

Shay L, Mariano AJ, Jacob SD, Ryan EH (1998) Mean and near-inertial ocean current response to hurricane gilbert. J Phys Oceanogr 28(5):858–889. https://doi.org/10.1175/1520-0485(1998)028

Shu Y, Pan J, Wang D, Chen G, Sun L, Yao J (2016) Generation of near-inertial oscillations by summer monsoon onset over the South China Sea in 1998 and 1999. Deep Sea Res I 118:10–19. https://doi.org/10.1016/j.dsr.2016.10.008

Sun Z, Hu J, Zheng Q, Li C (2011a) Strong near-inertial oscillations in geostrophic shear in the northern South China Sea. J Oceanogr 67(4):377–384. https://doi.org/10.1007/s10872-011-0038-z

Sun ZY, Hu J, Zheng Q, Li C (2011b) Strong near-inertial oscillations in geostrophic shear in the northern South China Sea J Oceanogr 67(4):377–384. https://doi.org/10.1007/s10872-011-0038-z

Sun B, Lian Z, Yuan Y, Xu H (2019) Seasonal variability of the wind-generated near-inertial energy flux in the South China Sea. Acta Oceanol Sin 38(4):136–145. https://doi.org/10.1007/s13131-018-1338-6

Sykulski AM, Olhede SC, Lilly JM, Early JJ. (2015). On parametric modelling and inference for complex-valued time series. arXiv:1306.5993. Retrieved from https://ui.adsabs.harvard.edu/abs/2013arXiv1306.5993S

Sykulski AM, Olhede SC, Lilly JM, Danioux E (2016) Lagrangian time series models for ocean surface drifter trajectories. J R Stat Soc C Appl 65(1):29–50. https://doi.org/10.1111/rssc.12112

Veneziani M, Griffa A, Reynolds AM, Mariano AJ (2004) Oceanic turbulence and stochastic models from subsurface lagrangian data for the northwest atlantic ocean. J Phys Oceanogr 34(8):1884–1906

Wang D, Hong B, Gan J, Xu H (2010) Numerical investigation on propulsion of the counter-wind current in the northern South China Sea in winter. Deep Sea Res I 57(10):1206–1221. https://doi.org/10.1016/j.dsr.2010.06.007

Wu CR, Hsin Y-C, Chiang T-L (2015) Seasonal and interannual changes of the kuroshio intrusion onto the east China sea shelf. J Geophys Res Oceans 119(8):5039–5051. https://doi.org/10.1002/2013JC009748

Yuan DL, Han WQ, Hu DX (2006) Surface kuroshio path in the luzon strait area derived from satellite remote sensing data. J Geophys Res Oceans. https://doi.org/10.1029/2005jc003412

Zheng Q, Lin H, Meng J, Hu X, Song YT, Zhang Y et al (2008) Submesoscale ocean vortex trains in the luzon strait. J Geophys Res. https://doi.org/10.1029/2007jc004362